Bulk and porous metastable beta Ti-Nb-Zr(Ta) alloys for biomedical applications

Brailovski, V.; Prokoshkin, S.; Gauthier, M.; Inaekyan, K.; Dubinskiy, S.; Petrzhik, M.; Filonov, M.

Publisher's version / Version de l'éditeur:
https://doi.org/10.1016/j.msec.2010.12.008
Materials science and engineering, 31, 3, pp. 643-657, 2011-01-01

Materials Science and Engineering C 31 (2011) 643–657

Contents lists available at ScienceDirect

Materials Science and Engineering C

journal homepage: www.elsevier.com/locate/msec

Bulk and porous metastable beta Ti–Nb–Zr(Ta) alloys for biomedical applications

V. Brailovski [a,*], S. Prokoshkin [b], M. Gauthier [c], K. Inaekyan [a], S. Dubinskiy [a,b], M. Petrzhik [b], M. Filonov [b]

[a] École de Technologie Supérieure, 1100, Notre-Dame Street West, Montreal (Quebec), Canada H3C 1K3
[b] National University of Science and Technology "MISIS", Leninskiy prosp. 4, Moscow 119049, Russian Federation
[c] Industrial Materials Institute (IMI), National Research Council, Government of Canada, 75, de Mortagne, Boucherville (Québec), Canada J4B 6Y4

ARTICLE INFO

Article history:
Received 14 June 2010
Received in revised form 7 October 2010
Accepted 21 December 2010
Available online 1 January 2011

Keywords:
Titanium biomedical alloys
Thermomechanical processing
Low-modulus
Metallic foams
Superelasticity

ABSTRACT

In this work, metastable beta Ti–Nb–Zr(Ta) ingots were manufactured by vacuum arc melting. The ingots thus obtained were divided into two batches: the first subjected to cold rolling (CR) from 30 to 85% of thickness reduction and subsequent annealing in the 450 to 900 °C temperature region, and the second atomized to produce 100 μm size powders. This powder was used to manufacture open-cell porous material. Regardless of the CR intensity, Ti–(18…20)Nb–(5…6)Zr (at.%) samples subjected to 600 °C (1 h) annealing showed a significant material softening due to the stress-induced martensitic transformation. The Young's modulus of these alloys varied between 45 and 55 GPa, and the yield stress, between 300 and 500 MPa. The obtained Young's moduli, which are comparable to 55–66 GPa of concurrent beta-titanium alloys and 45–50 GPa of superelastic Ti–Ni alloys, come close to those of cortical bones. Compression testing of the porous material as a function of porosity (from ~45 to 66%) and interconnected cell size (d_{50} from 300 to 760 μm) showed the following properties: Young's modulus from 7.5 to 3.7 GPa, which comes close to that of trabecular bones, and ultimate compression strength, of from 225 to 70 MPa.

1. Introduction

While one of the major applications for metallic implants is the replacement of worn or damaged bones, one of the major drawbacks of implants made of conventional materials is the marked difference between the mechanical behavior of the implant and that of bone. Metallic implants have a much higher stiffness and their merely linear stress–strain characteristics do not match the plateau-like hysteretic behavior of bones, which results in implant loosening. Titanium–nickel near-equiatomic alloys manifest the so-called superelastic behavior, which is quite similar to that of living tissues, and therefore represents an excellent candidate for implant material capable of mimicking the mechanical behavior of bone [1,2].

Even though the majority of studies have neither definitely established the position of Ti–Ni among the metallic biomaterials, nor confirmed its ultimate cyto-compatibility, governing instances and the scientific community remain very reluctant to endorse the use of Ti–Ni alloys — despite the significant number of Ti–Ni implants currently on the North American market, including bone plates, stents and the like. Indeed, the fact that Ti–Ni contains approximately 50% nickel, which is considered a toxic and even carcinogenic element, represents the strongest argument against its use as an implant material because of a possible release of nickel in the human body and the potential danger to a patient's overall health [3].

The need for a metallic implant material combining superelasticity with biocompatibility comparable to that of pure titanium represents the main incentive for ongoing research in the field of β-type Ti-based superelastic alloys. Ternary and quaternary Ti–Nb-based alloys have been extensively investigated during the last several years and the results confirm the possibility of producing Ni-free, Ti-based alloys with superelasticity thanks to reversible β to α″ martensitic transformation [4–10]. These materials have joined the family of the previously-developed low-modulus near-β and β-type titanium alloys containing non-toxic elements such as Nb, Ta, and Zr, but without superelasticity [11,12]. The low elastic modulus of these alloys is caused by the fact that the elastic modulus of the body-centered cubic (bcc) β phase is lower than that of the hexagonal close-packed (hcp) α phase.

To provide a way for living bone to attach itself permanently to an implant, an artificial bone should have a porous structure. It has been proven that porous titanium implants demonstrate an important gain in promoting tissue ingrowth and in the firm securing of an implant [13,14]. Several manufacturing techniques are capable of producing porous materials, such as sintering, self-propagating or combustion synthesis (SHS), freeform fabrication, etc. Some recent studies show the potential of using these techniques to control pore size, shape, orientation and distribution, including the creation of hierarchical and functionally-graded pore structures [15–17].

The problem of producing porous Ni-free Ti-based superelastic implant material mimicking the mechanical behavior of bone and with biochemical affinity to osteogenesis is extremely challenging and remains unsolved to this day. The first challenge consists in the

* Corresponding author. Tel.: +1 514 396 8800/8594; fax: +1 514 396 8530.
E-mail address: vbrailovski@mec.etsmtl.ca (V. Brailovski).

0928-4931/$ – see front matter © 2010 Elsevier B.V. All rights reserved.
doi:10.1016/j.msec.2010.12.008

medium-scale manufacturing of the selected Ti–Nb–Ta/Zr superelastic alloys. Until now, these materials have been produced in very limited quantities (20-gram buttons) using laboratory arc melting furnaces. The minimum quantity of feedstock material needed for powder production is about 5 kg, which means that the laboratory technology must be scaled-up, with all the difficulties inherent to this type of scaling. The second challenge resides in the manufacturing of porous Ti–Nb–Ta/Zr superelastic alloy with controlled porosity suitable for orthopedic applications.

Generally speaking, shape memory effects including superelasticity are observed in titanium alloys where alloying elements act as beta-stabilizers to promote $\beta \rightarrow \alpha''$ phase transformation. The beta-stabilizers can be categorized into three groups:

1. Elements that are isomorphous to β-Ti and form continuous solid solutions with limited solubility in α-phase: Ta, Nb, V and Mo;
2. Elements that form continuous solid solutions in α- and β-Ti: Zr and Hf; and
3. Elements with a limited solubility in both α- and β-Ti which form intermetallic compounds: Mn, Cr, Fe, Cu, Ni, Si, and Co.

Tantalum and niobium are considered to be the strongest beta-stabilizers, effectively decreasing Young's modulus of titanium alloys [18–20]. Zirconium, if taken individually, is considered as a neutral or weak beta-stabilization element: contrary to Ti–Nb or Ti–Ta binary alloys, Ti–Zr alloys do not manifest shape memory. However, Zr begins to play a role of an effective beta-stabilizer when it is combined with Nb or Ta [19].

Considering the previous remarks, the alloying of binary Ti–Nb alloys with a third element, such as Ta or Zr, is done with the goals of stabilizing the β phase at room temperature, to create conditions of α'' phase formation, to decrease Young modulus, and to promote solid solution hardening, thus improving the Ni-free titanium alloys' shape memory properties. In this work, both Ti–Nb–Ta and Ti–Nb–Zr alloys are concurrently studied during the first phase of the project: manufacturing and thermomechanical processing of bulk material. For the second phase, fabrication of the porous material, one of the two alloys is selected based on its overall quality, including the homogeneity of the produced ingots.

2. Materials and methods

2.1. Casting

Ti–Nb–Ta ingots (50 mm diameter, 15 mm thick) were cast in GIREDMET (Russia) by arc-melting in Ar-atmosphere (1 bar) with a non-consumable W-electrode in a water-cooled Cu crucible. After casting, the ingots were subjected to homogeneous annealing at 900 °C in a vacuum furnace. Ti–Nb–Zr ingots (50 mm diameter, 660 mm long) were manufactured by Flowserve Corp. (USA). The Vacuum Arc Remelting (VAR)-prepared ingots were subjected to Hot Isostating Pressing (HIP) prior to delivery. The chemical compositions of these Ti–Nb–Zr(Ta) alloys are presented in Tables 1 and 2.

2.2. Thermomechanical processing of bulk material

The Ti–Nb–Zr and Ti–Nb–Ta ingots were Electrical Discharge Machining (EDM)-cut in $1\times1.5\times100$ (mm) and $2\times15\times50$ (mm) strips, respectively, and subjected to thermomechanical processing (TMP): cold rolling (*FENN* four-high rolling mill) and post-deformation annealing (*PYRADIA*) followed by water-quenching. The following TMP conditions were applied: Ti–18.1Nb–5Zr (at.%): cold rolling (CR) $e=0.27$–0.47, 0.75 and 2.75; Ti–20.5Nb–5.6Zr: $e=0.37$ and 2; Ti–20.8Nb–5.5Zr: $e=0.3$ and 2; Ti–19.5Nb–6.5Ta, Ti–21Nb–7Ta: $e=0.3$; with subsequent annealing at 450, 600, 750 (all 1 h) and 900 °C (0.5 h).

Table 1
Chemical composition of Ti–Nb–Ta ingots (GIREDMET, Russia).

Element	Ingot 1, at.%	Ingot 2, at.%	Ingot 3, at.%
Ti	74	73	72
Nb	19.5	20.2	21
Ta	6.5	6.8	7

Table 2
Chemical composition of Ti–Nb–Zr ingots (Flowserve, USA).

Element	Target composition, at.%	Ingot 1, at.%	Ingot 2, at.%	Ingot 3, at.%	Ingot 4, at.%
Ti	72	75.7	74.9	71.8	72.6
Nb	22	18.1	18.0	20.8	20.5
Zr	6	5.0	4.9	5.5	5.6

2.3. Foam manufacturing

Two batches of Ti–Nb–Zr powder were produced from Ti–Nb–Zr alloy ingots by TLS Technik Spezialpulver (Germany): the first batch was produced by atomizing ingots 1 and 2, while the second batch was obtained using ingots 3 and 4 atomization feedstock (see Fig. 1). Titanium alloy foam samples with three target densities (≈50, ≈55, and ≈65%) were manufactured using a novel powder metallurgy process [21]. Chemical compositions of the first batch of powder and foams (ingots $1+2$) and of the second batch of powder and foams (ingots $3+4$) are presented in Table 3. The Ti, Nb, and Zr contents were measured using Inductively-Coupled Atomic Emission Spectrometry (ICAP-AES, ASTM E1479) and Direct Current Plasma Atomic Emission Spectrometry (DCP-AES, ASTM E1097) techniques.

Fig. 2 collects the content of oxygen, carbon, nitrogen and hydrogen in bulk, powder and foam specimens. The H, O, and N contents were measured using the Inert Gas Fusion (IGF, ASTM E1447 and E1409) technique and C content was measured using chemical analysis in conformance with ASTM E1941.

To produce foam, spherical-shaped Ti–Nb–Zr powders with an average diameter of 100 μm were dry-mixed with an organic binder and a foaming agent, all in powdered form. The final pore size of the titanium foams was controlled through blend composition. The homogenous mixture was then moulded in the stainless steel tubular moulds (15 mm diameter, 50 mm long), and subjected to a three-step heating process including: a) foaming at 200 °C, b) decomposition of the polymeric binder at 425 °C (both in the re-purified argon atmosphere, 1×10^{-10} ppm O_2), and c) vacuum sintering at 1400 °C (1×10^{-6} Torr) for 1 to 4 h. The density of each foam specimen was measured using gravimetric and volumetric measurements. An average pore size was measured using X-Ray Tomographic analysis. The main phases of the foam manufacturing technology are illustrated in Fig. 1.

2.4. Analysis and characterization

Metallographic imaging (Metallovert, LEITZ) was carried out on bulk alloys, powder particles and foams.

X-Ray Tomographic analyses were carried out on cylindrical Ti–Nb–Zr foam specimens (~11 mm diameter × ~14 mm high) using an XTek HMXST 225 system with cone beam configuration having a 140 kV, 64 μA point source and a PerkinElmer 1621AN CsI flat panel detector (2000 × 2000 pixels, 400 mm × 400 mm, 200 μm/pixel). A 0.5 mm Cu filter was used, while the distance from source to object was 560.7 mm. The scanning parameters were: 1 s/frame, 1 frame/projection and ~3000 projections/specimen. The resolution of 3D scans is 6.4 μm.

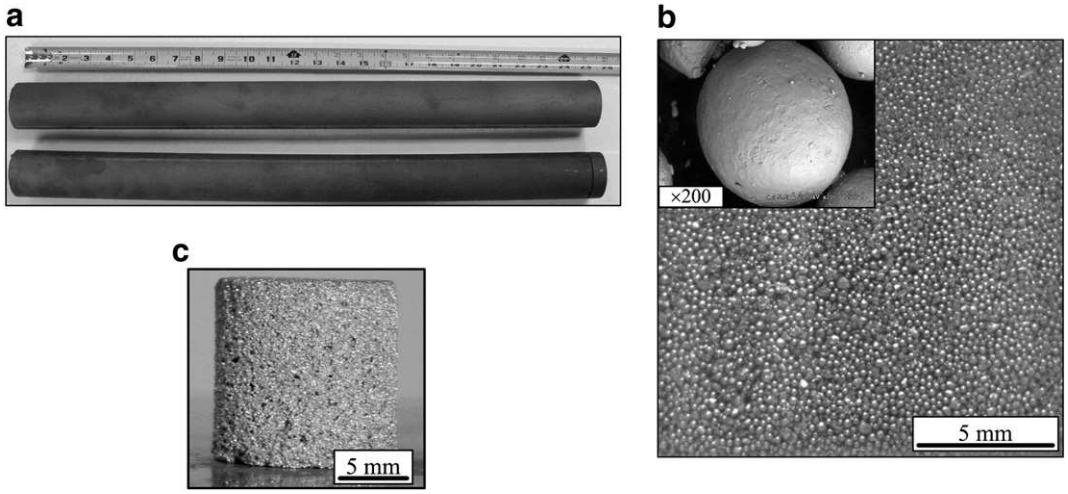

Fig. 1. Ti–Nb–Zr foam manufacturing: a) ingots (Flowserve, USA); b) powder (TLS, Germany) and c) foam (IMI-NRC, Canada).

Image analyses of 2D cross-sections of foams acquired through tomography were performed using a Clemex Vision PE 3.5 (Clemex Technologies, Canada).

Helium gas pycnometry was carried out to determine the percentage of closed-porosity in the foam samples. The apparatus used was an AccuPyc 1330 Helium Gas Pycnometer (Micromeritics).

Transmission electron microscopy (TEM) analysis (JEM 200CX, JEOL) was performed on bulk Ti–Nb–Zr samples subjected to CR and post-deformation annealing. Thin foils for TEM were prepared from 0.1 mm-thick platelets by electropolishing at −38 °C using 15% HNO_3 spirit solution and "TENUPOL-5" equipment (Struers, Denmark).

X-ray analysis was performed using a PANALYTICAL X'Pert Pro diffractometer at different temperatures including cooling down to −150 °C. The samples for X-ray analysis were mechanically polished and chemically etched using an acid solution of the following composition: $2HF:1HNO_3:17H_2O$.

Microhardness measurements were performed at room temperature (RT) using an INSTRON Wilson Tukon 2100 (Microhardness Vickers, HV, 500 g, 10 s) and a Nano-Hardness Tester, CSM (Switzerland).

Isothermal tensile testing at temperatures of −18, 25, 37, 75 and 200 °C was carried out using a custom-made tensile testing bench and MTS' MiniBionix at −35, −20, 0, 25, 60 and 100 °C.

Compression testing with simultaneous video recording was performed on porous samples using MTS' Alliance RF/200 ($\xi = 0.0017\ s^{-1}$) following three modes: (a) monotonous compression up to a nominal strain of 55%; (b) cyclic compression up to a maximum fixed strain of 5%; and (c) cyclic compression with incrementally increased strain up to specimen failure.

Shape recovery bending testing was carried out with selected bulk samples after conventional and severe plastic deformations. The samples were bent around cylindrical mandrels of different radii, heated in boiling water or by hot air up to 250 °C (heat gun) and the recovery strain was then measured using an optical comparator technique.

Table 3
Chemical composition of Ti–Nb–Zr foams from ingots 1 + 2 and 3 + 4.

Component	Powder from ingots 1 + 2, at.%	Foams from ingots 1 + 2, at.%	Powder from ingots 3 + 4, at.%	Foams from ingots 3 + 4, at.%
Ti	78.3	78.5	73.9	73.3
Nb	16.3	16.9	21.0	20.9
Zr	4.7	4.8	5.2	5.5

3. Results

3.1. Bulk alloys

3.1.1. Microstructure

X-ray analyses of both alloys (Ti–Nb–Zr/Ta) and TEM of the Ti–Nb–Zr alloy after different TMP routes determined that the majority of the Ti–Nb–X alloys' structure is β-austenite (bcc). However, important quantities of α (hcp) and α″ (orthorhombic lattice) martensites are present (Fig. 3). Note that the ω-phase (hcp) is not seen on these

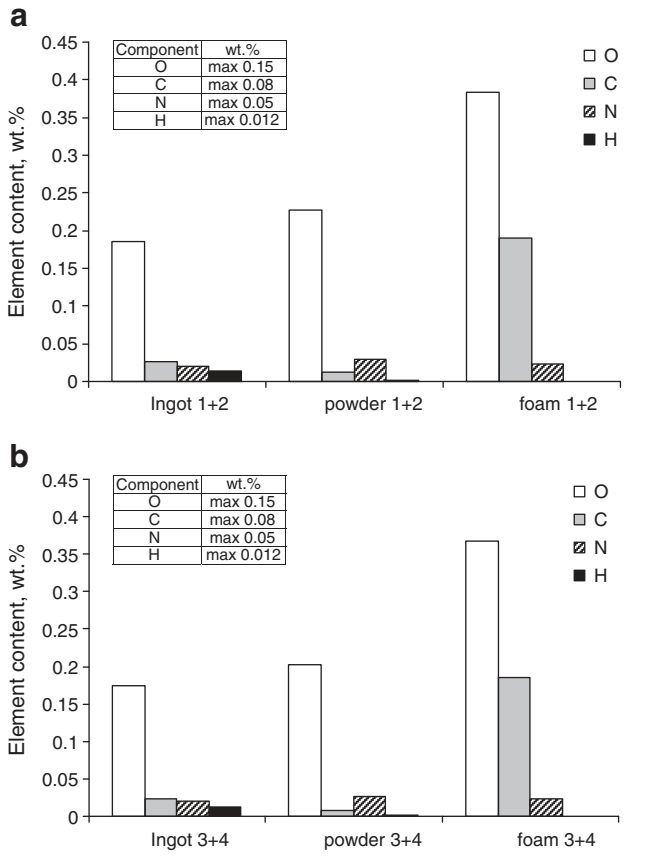

Fig. 2. Oxygen, carbon, nitrogen and hydrogen contents in bulk, powder and foam specimens: a) ingots 1 + 2, and b) ingots 3 + 4. Insets contain maximum concentrations according to ASTM F67-00 (Grade 1).

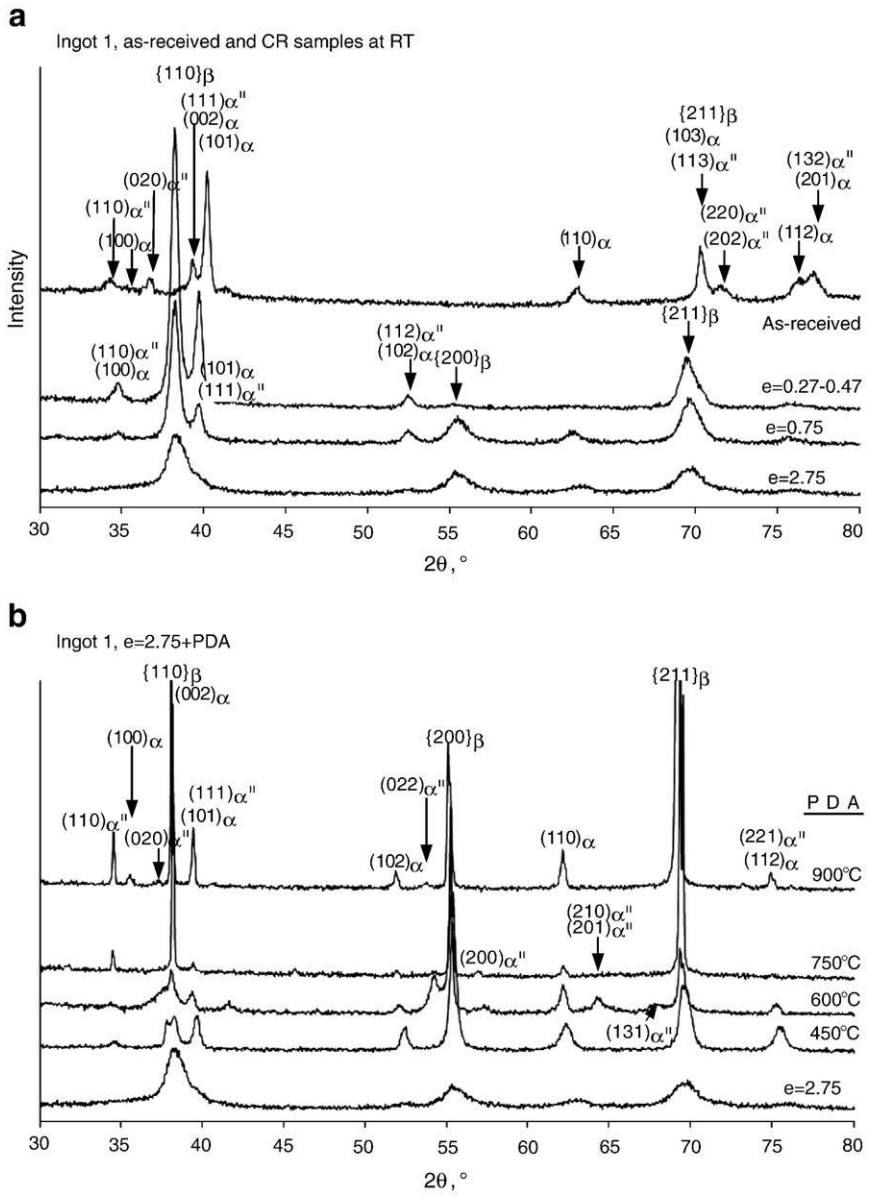

Fig. 3. Ti–18.1Nb–5Zr alloy, X-ray analysis: a) as-received and CR; and b) CR (e = 2.75) and annealed (450–900 °C).

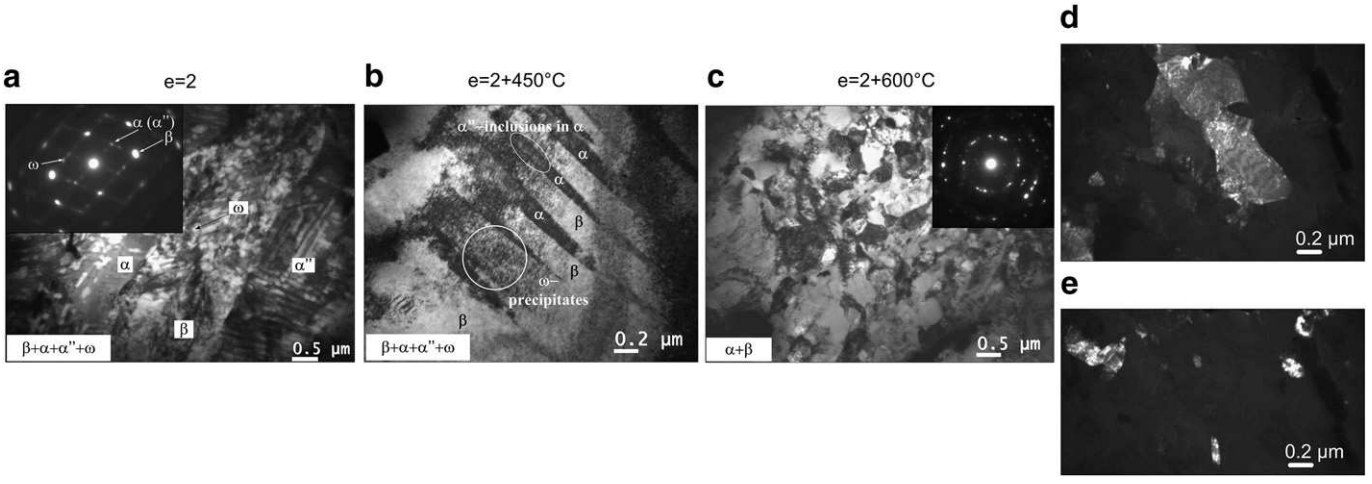

Fig. 4. TEM images of Ti–20.8Nb–5.5Zr alloy subjected to: a) CR, e = 2 — bright field image and electron diffraction pattern, <110>$_\beta$ zone axis; b) CR, e = 2 + 450 °C — bright field image; c) CR, e = 2 + 600 °C — bright field image, electron diffraction pattern, d) dark field image, β-phase, and e) dark field image, α-phase.

diffractograms, but it is present in the structure, as shown by TEM (see Fig. 4).

The accumulation of plastic deformation during CR initiates reverse martensitic transformation to β-austenite (Fig. 3a) [22–24]. Post-deformation annealing (PDA) at 450–750 °C after conventional, moderate and severe CR (0.27–0.47; 0.75; 2–2.75) does not change a phase state: α, α″ phases are observed in both cases, but with different proportions. The higher the PDA temperature, the greater the quantity of α and α″ phases, with the exception of annealing at 900 °C, which results in an increase of the β-austenite line's intensities and a decrease of the α and α″ lines' intensities — some lines are no longer visible, which could reflect changes in material texture (Fig. 3b). Note that after severe CR and annealing at 900 °C, the quantity of α and α″ phases is greater than after conventional CR.

Generally speaking, the higher the annealing temperature, the narrower the $\{110\}_\beta$ line, which is the result of recovery, polygonization and recrystallization. Recrystallization of the work-hardened alloy, which starts at 600 °C, results in very fine grain and subgrain structure. Note that severe plastic deformation (e = 2.75) did not lead to material amorphization, contrarily to Ti–Ni shape memory alloys [25]. TEM allows clear observation of the β, α, α″ and ω phases in the severely deformed (e = 2) and annealed (450 °C) alloy, as indicated in Fig. 4a,b (β-austenite is the principal phase); the ω phase appears mostly after 450 °C; the α″ phase 100 nm width plates can be observed inside β-austenite grains. After 600 °C annealing, only β and α phases can be identified with certitude (Fig. 4c,d,e); α″ and ω phase observations after this treatment are complicated by the very fine grain–subgrain structure of the alloy.

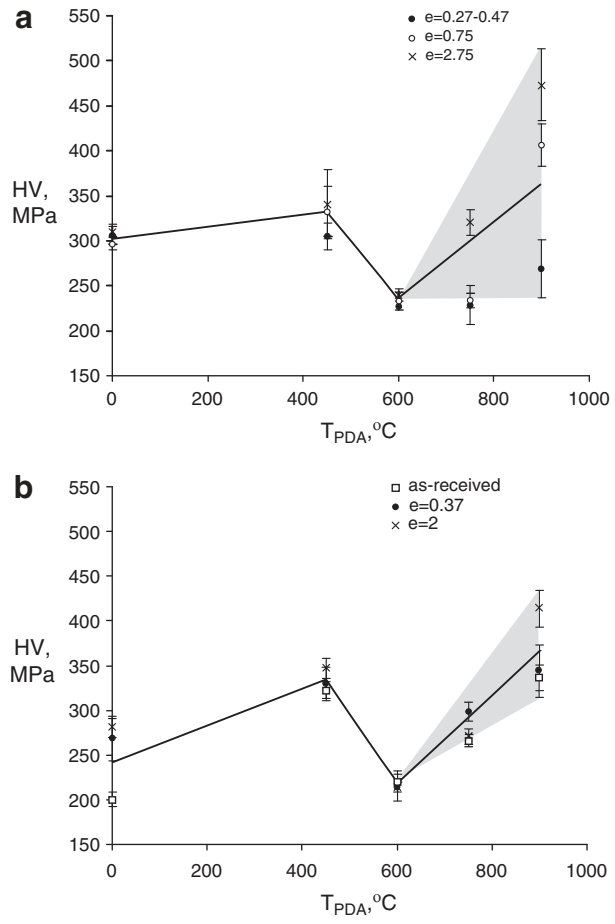

Fig. 5. Vickers microhardness as a function of CR intensity and annealing temperature: a) Ti–18.1Nb–5Zr, and b) Ti–20.5Nb–5.6Zr. Grey-shaded zones illustrate large scatter of data at $T_{PDA} > 600$ °C.

3.1.2. Mechanical behavior

Microhardness measurements performed at RT on Ti–Nb–Zr specimens show strong softening after annealing at 600 °C after all levels of CR (Fig. 5).

Tensile testing of Ti–Nb–Zr alloy samples was performed after different TMP routes. Stress–strain diagrams are shown in Fig. 6. For Ti–20.5Nb–5.6Zr specimens (ingot 4), recoverable strain during unloading (including SE and elastic strains) at RT is equal to ≈1.5% (for induced stain of 2.4%) (Fig. 6a,b). Partial superelasticity (Fig. 6a, b) and variations of the apparent yield stress with testing temperature (inset in Fig. 6b) indicate the presence of the stress-induced phase transformation. The transformation yield stress–temperature slope is $\Delta\sigma/\Delta T \approx 2$ MPa/°C, which is close to that observed in Ref. [5]. Note that samples annealed at 450 °C after e = 0.37 demonstrate brittle behavior (Fig. 6b), which is a result of the combined effect of strain hardening and precipitation of the ω-

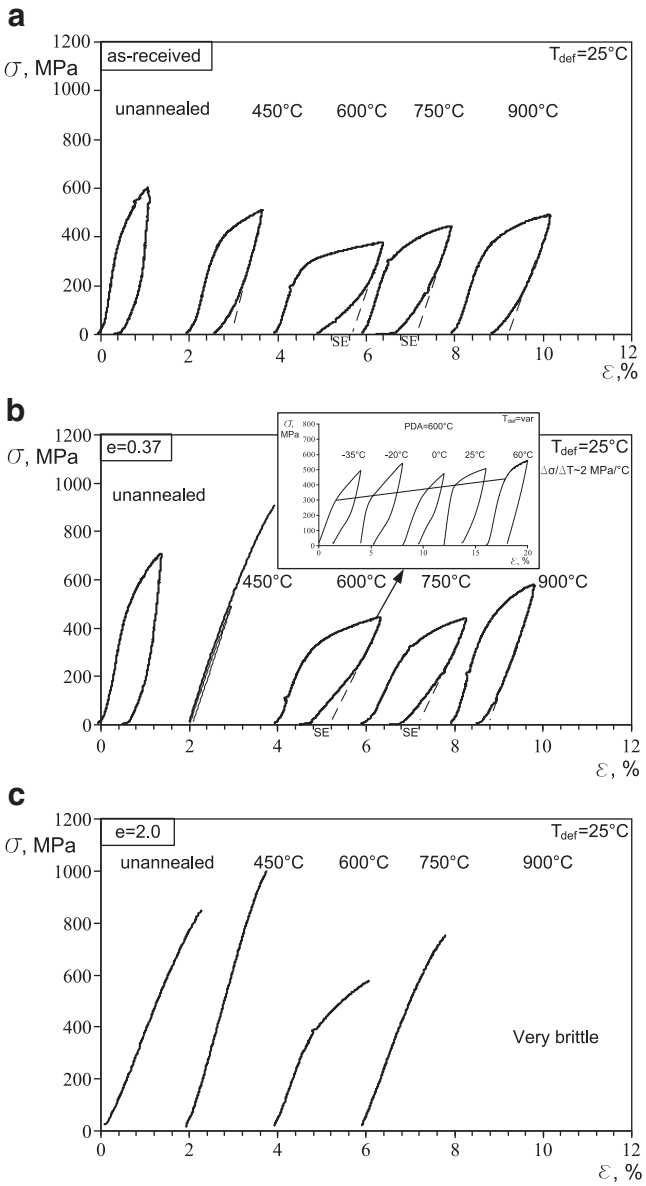

Fig. 6. Stress–strain diagrams of Ti–20.5Nb–5.6Zr alloy annealed at 450–900 °C: a) as-received, b) CR, e = 0.37, and c) CR, e = 2.0. Inset contains isothermal stress–strain curves obtained at different testing temperatures after e = 0.37 + 600 °C.

phase, the latter is the strongest in the 400–450 °C temperature range [4]. In the case of severe CR, the alloy becomes brittle, as seen in Fig. 6c.

Similarly to Ti–Nb–Zr, Ti–Nb–Ta alloy demonstrates partial superelasticity in the vicinity of RT, especially after annealing at 600 and 750 °C (Fig. 7a). When the deformation temperature increases, transformation yield stress increases accordingly, $\Delta\sigma/\Delta T \approx 1.7$ MPa/°C (Fig. 7b). The $\beta \rightarrow \alpha''$ phase transformation in the e = 0.26 + 600 °C specimens is triggered by deformation, as seen on X-ray diffractograms taken from specimens tested at 25 and 75 °C (Fig. 7c,d).

Shape memory recovery strain bending experiments were performed at RT with Ti–Nb–Zr samples subjected to CR and PDA (ingots 1 and 4). Severely deformed samples (e = 2) showed better shape recovery than conventionally deformed samples (e = 0.37), but this effect was very weak (about 0.5%, heating up to 250 °C).

3.2. Ti–Nb–Zr foams

3.2.1. Microstructure

Metallographic analysis was performed on powder particles and foams produced from ingots 1 + 2 (Fig. 8). Polycrystalline structure in the spherical (a, b) as well as in the irregular (c) particles was observed with grain size of 10–20 μm, which is much smaller than in the initial bulk material (300–400 μm).

Tomographic analysis was carried out on a cylindrical Ti–Nb–Zr foam specimen for each of the three formulations, leading to three different porosities. These 3D scans were then used to produce 2D cross-sections, which were processed to obtain the pore size distribution of the samples (Fig. 9). Ten different cross-sections were analyzed for each of the given foams. The relevant data extracted from these analyses (d_{10}, d_{50} and d_{90} correspond to 10, 50 and 90% of the pores' distribution) are compiled in Table 4.

Also included in Table 4 are the results of Helium pycnometry analyses which were performed on the samples that had been submitted to tomographic scans. The pycnometry results enabled the amount of open and closed porosities within the Ti–Nb–Zr foams to be calculated.

The irregular pore shape and wide pore size distributions of the Ti–Nb–Zr foams are clearly apparent from Fig. 9a,b,c. The graphed pore size distributions (Fig. 9d,e,f) also show that decreasing foam porosities result in more "bell-shaped" distributions of pore diameters, with a lesser fraction of the very large pores. The d_{50} values for the pore size distributions decrease with decreasing foam porosity (Table 4), going from 760 μm for the 65.15% porous foam to 306 μm in the case of foam with 45.84% porosity. These pore size distributions ensure that a wide range of pores have dimensions that are favorable for bone growth into the foam structures. It is known that pore sizes in the approximate range of 200 to 600 μm result in a rapid bone formation [26–28]. The lower pore size limit is related to the size of cells (~50 μm), while the upper pore size limit is related to the availability of binding sites and the anatomic dimensions of the pores of the specific bone tissue to be replaced. The foams also comprise a certain amount of micron-sized porosity which was not taken into account by the image analysis, as the tomographic images were generated with a resolution of 6.4 μm.

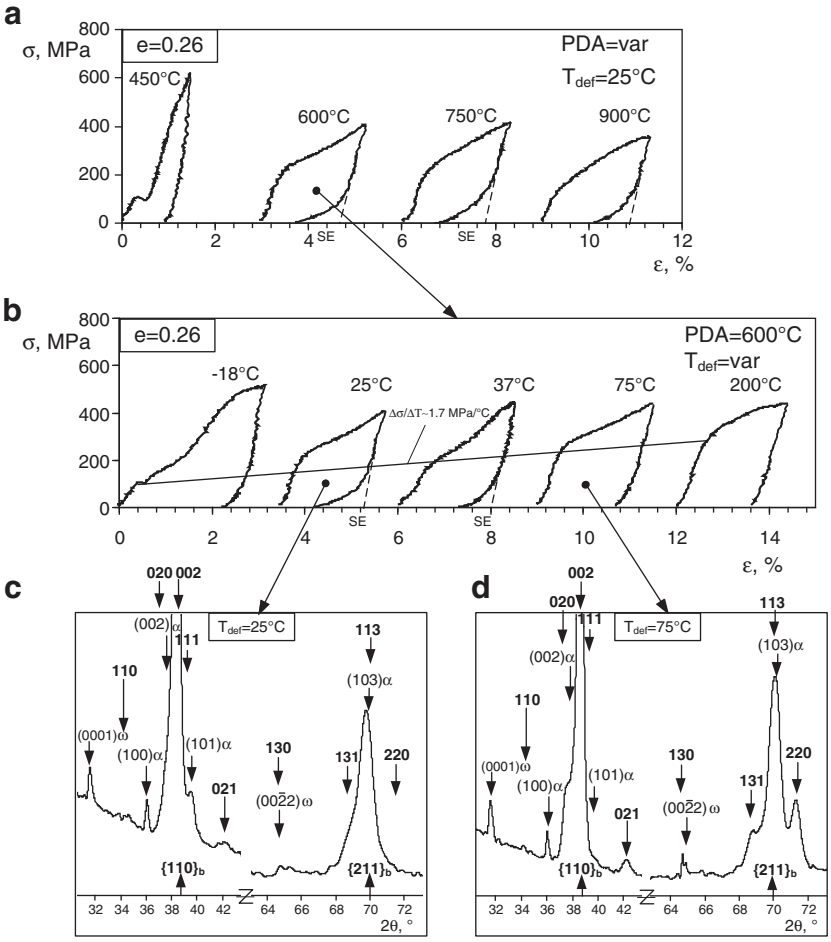

Fig. 7. Stress–strain diagrams of Ti–19.5Nb–6.5Ta alloy: a) e = 0.26 + annealing in the 450–900 °C temperature range, b) testing at different temperatures after e = 0.26 + 600 °C, and RT X-ray diffractograms of e = 0.26 + 600 °C specimens after mechanical testing at 25 °C (c) and 75 °C (d) (indexes in bold correspond to α″ phase).

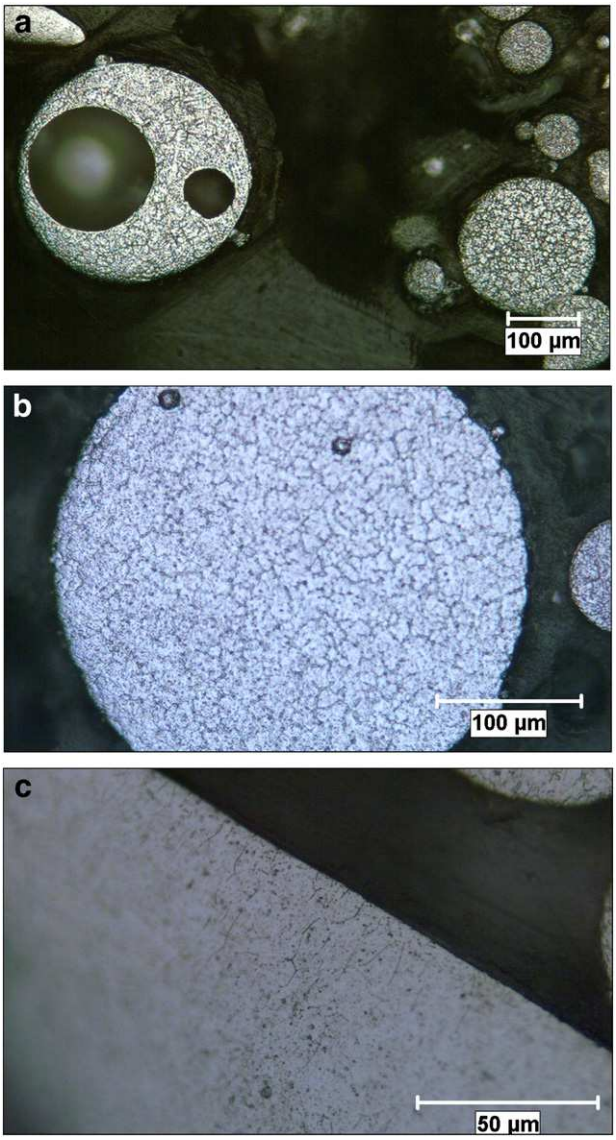

Fig. 8. Metallography of powder particles (a, b, c) (ingots 1 + 2).

The He-gas pycnometry results (Table 4) also demonstrate that only a very small fraction of the total porosity of each foam is closed porosity. This indicates that bone cells will have access to most of the pore volume to allow the cells' ingrowth, vascularization and diffusion of body fluids.

3.2.2. Mechanical behavior

Note that in this section "*" superscript indicates foam properties: apparent Young's modulus E^*, apparent compressive strength CS^* (analog UTS) and plateau stress σ^* (analog YS).

Mechanical compression testing was performed on the as-received porous samples:

(a) Monotonous compression up to a nominal strain of 55% with simultaneous video recording allowed identification of three deformation stages (Fig. 10): I. No visible damage; II. Visible cracks; and III. Densification and fragment detachment;
(b) Cyclic compression up to a maximum fixed strain of 5% did not result in visible specimen damage (Fig. 11);
(c) Cyclic compression with incrementally increased strain up to specimen failure showed that in the case of the most dense specimen (45.06%), produced from ingots 3 + 4 (Fig. 12), apparent yield stress continuously increases with increasing strain. The same results were obtained with the foams produced from ingots 1 + 2.

4. Discussion

4.1. Bulk alloys

4.1.1. Microstructure

Conventional and moderate CR followed by post-deformation annealing at 750 and 900 °C form a bi-modal structure containing large grains composed of smaller constituents, which could be grains or subgrains. It seems that the large grains contain traces of the initial grain structure (grain boundary hereditary effect) and, therefore, small structural elements are indeed newly-formed grains and not subgrains. The final conclusion can be made after a detailed TEM analysis. During subsequent annealing, severe plastic deformation results in a homogeneous 50 μm grain structure (Fig. 13b), which is significantly finer than that of the as-received state (100–500 μm, Fig. 13a).

X-ray analysis of all of the tested alloys (Ti–Nb–Ta/Zr) shows that β-austenite is a dominant phase, and that the integral width of X-ray lines (only separated β-austenite lines) decreases with an increase in annealing temperature; annealing at 600 °C corresponding to the alloy's recrystallization development regardless of the thermal and thermomechanical treatments (Fig. 14). It should be noted that thermally induced β↔α″ phase transformation was not directly observed using the X-ray technique in the −150 + 400 °C temperature range, possibly because of limitations related to the precision of the apparatus used. Note also that for these alloys, the Differential Scanning Calorimetry (DSC) technique is not useful for detection of thermally-induced transformation [29]. However, this transformation was stress-induced during the mechanical testing of this material at different temperatures.

4.1.2. Mechanical behavior

The mechanical behavior of Ti–Nb–X alloys depends not only on the size of the structural elements, but also on the quantity of the phases (β, α, α′, α″, and ω) and on the solid–solid phase transformations. Minimum HV is reached after annealing at 600 °C regardless of the CR conditions, and this minimum coincides with the minima in yield stress and Young's modulus (Fig. 15a,b,c). After severe plastic deformation (e = 2), YS and E measurements result in a large scattering of the results obtained, due to the numerous surface cracks (Fig. 15c).

It is well known that HV, YS and E (the latter to a smaller extent) are structure-sensitive parameters, and therefore they can be influenced by grain and subgrain size, dislocation density, precipitates' size and distribution, phase state, and the difference between the temperature range of martenstic transformation and testing temperature.

Metallographic analysis of Ti–20.5Nb–5.6Zr alloy samples subjected to different TMPs allowed the observation of a conventional monotonous trend: for a given cold-work intensity, the higher the annealing temperature, the larger the grain size, which evolves in the 1 to 100 μm range. X-ray diffractometry analysis showed that the higher the annealing temperature, the smaller the dislocation density. To sum up, neither the grain size nor the dislocation density evolution can explain the HV, YS, and E (PDA) softening in the vicinity of 600 °C PDA.

It is known that Nb, Zr and H are β-stabilizers; and that N, O and C are α-stabilizers [30]. If we consider Ti–Nb–Zr alloy phase diagrams as a function of the alloy's temperature [31], then in the 600–900 °C range, the alloy has a fully austenitic structure with the maximum quantity of alloying elements in a β-matrix. When the alloy's temperature decreases, β→α transformation leads to the dual-

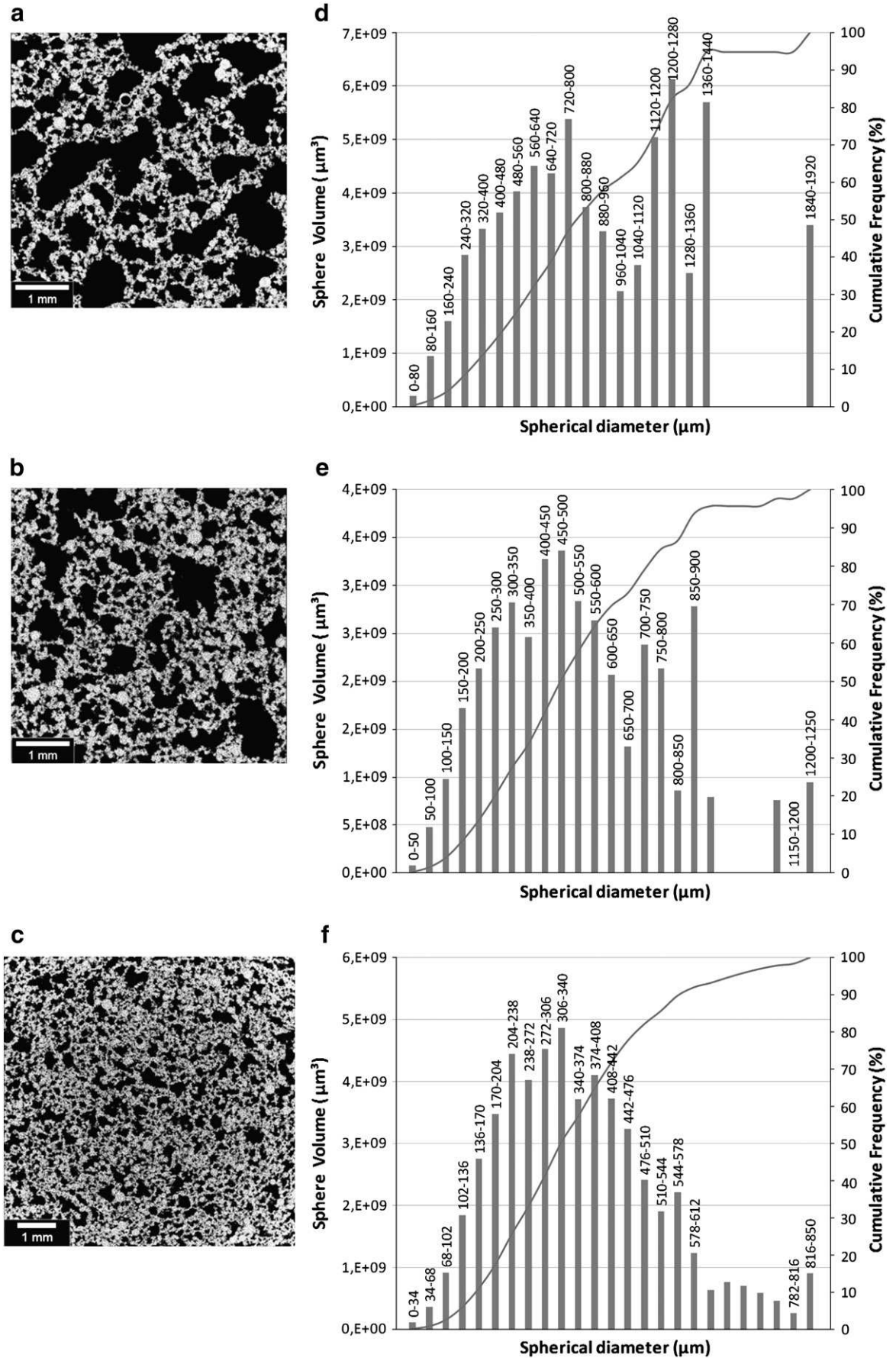

Fig. 9. Tomographic analyses of Ti–Nb–Zr foams: (a, d) 65.15%, (b, e) 55.13%, (c, f) 45.84%; (a, b, c) 2D cross-section and (d, e, f) pore size distribution.

Table 4
Pore size distribution data for Ti–Nb–Zr foams.

Foam porosity[a] (%)	Open (closed) porosity[b] (%)	Average foam porosity[c] (with standard deviation) (%)	Pore size distribution parameters[c]		
			d_{10} (μm)	d_{50} (μm)	d_{90} (μm)
65.15	64.43 (0.71)	63.4 ± 1.88	280	760	1320
53.13	54.39 (0.74)	55.73 ± 2.17	175	450	825
45.84	45.66 (0.18)	45.11 ± 1.02	136	306	561

[a] Calculated from sample dimensions and mass.
[b] From He-gas pycnometry.
[c] From Tomography/image analysis.

phase structure. In this case, the chemical composition of the β phase will be different from that at higher temperatures. Considering the phase diagram, 600 °C can be seen as a "threshold" temperature corresponding to the metastable austenite structure with the lowest lattice stability in respect to β→α and β→α″ transformations. This effect can result in phase transformation under stress, which would be macroscopically manifested as material softening. Note that a decrease in strength and Young's modulus caused by β→α transformation has already been observed [32].

For all annealing temperatures below 900 °C, the peak positions of the selected X-ray lines are shifted to greater angles, thus indicating a decrease in lattice parameter (Fig. 16). This trend can be explained by a decrease in alloying element solubility when temperature decreases [20]. In the two-phase region, a combined action of two phenomena leads to an elastic distortion of the austenite lattice: a) β-austenite phase Zr-impoverishment, and b) compressive stresses applied to β-austenite by an increasing fraction of α-martensite.

Annealing at 900 °C results in HV values which are similar to those measured in the as-received and cold-rolled samples (Fig. 5). The strength of the β phase (according to X-ray analysis, it is a major phase after annealing at 900 °C and water-quenching) will therefore depend on the solubility of the alloying elements. It seems that the effect from the solid-solution hardening is greater than that from the presence of the soft β phase, which is reflected not only by HV measurement, but also by the decreasing plasticity of the material during tensile testing, especially in the case of severe cold deformation.

After aging at temperatures in the region close to the dual-phase (aging at 600 °C corresponds to the β + α region where β dominates), strength correlates with the phases present in the alloy. If β transforms to α, the material should be hardened. However, this effect seems to be counteracted by a decrease in the alloying element's content in the β phase and by the possible phase transformation β→α (or α″) under stress (HV, tensile test). (It is known that material softening is observed when β→α″ transformation takes place [33]).

Annealing at 450 °C takes place in the α + β region, and after quenching, we have dual-phase α + β or even α + α″ + β structures of maximum strength. Moreover, the presence of ω-phase at these temperatures can further strengthen the material [34]. Finally, if at this temperature, the recovery process is not fully completed, it will also contribute to material strengthening.

Generally speaking, the higher the annealing temperature, the greater the quantity of β-phase, but the lower the dislocation density.

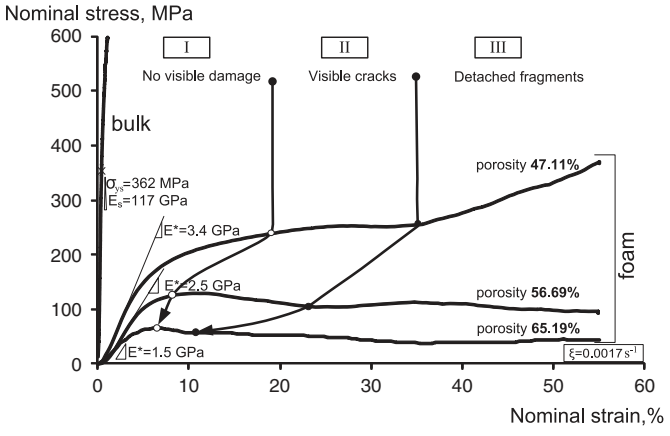

Fig. 10. Compression diagrams: deformation of Ti–Nb–Zr bulk and foam (ingots 1 + 2) specimens with different porosities (visible deformation stages).

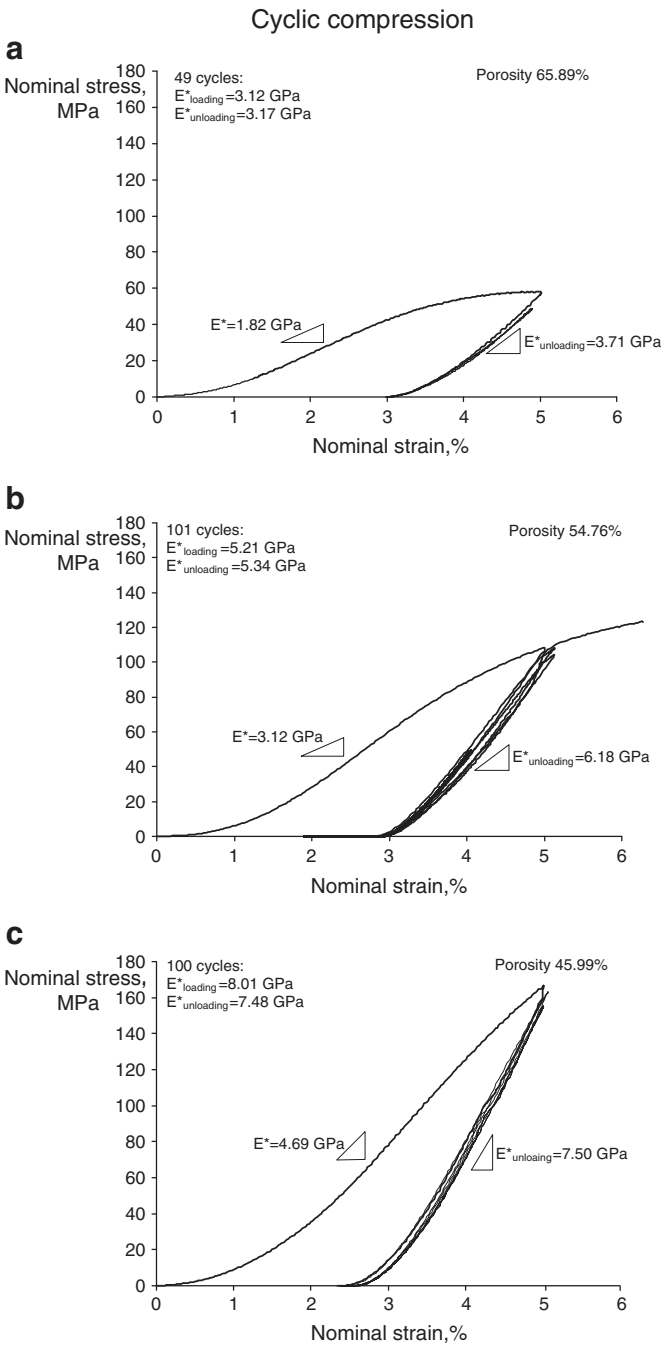

Fig. 11. Compression diagrams: cycling of Ti–Nb–Zr foams (ingots 1 + 2) with different porosities: a) 65.89%, b) 54.76%, and c) 45.99%.

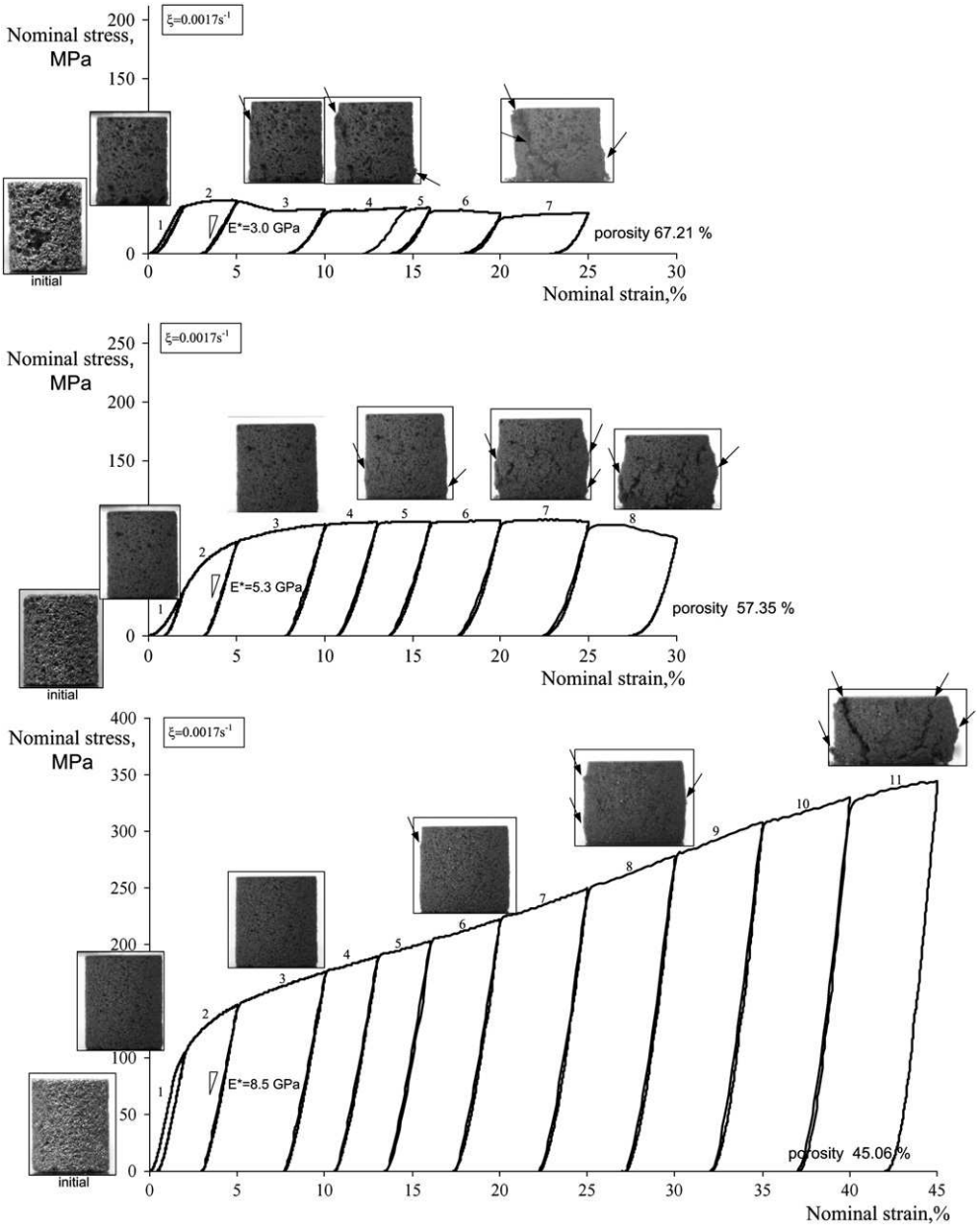

Fig. 12. Compression diagrams: cycling of Ti–Nb–Zr foams (ingots 3 + 4) (arrows — visible crack initiation).

If we consider the following correlation between Young's modulus and the phase state (without transformation) of $E_\omega > E_\alpha > E_{\alpha''} > E_\beta$ [35], the higher the annealing temperature, the greater the β-phase quantity, and therefore the softer the material. Similarly, we find that the higher the annealing temperature, the lower the dislocation density and therefore the softer the material. However, the higher the

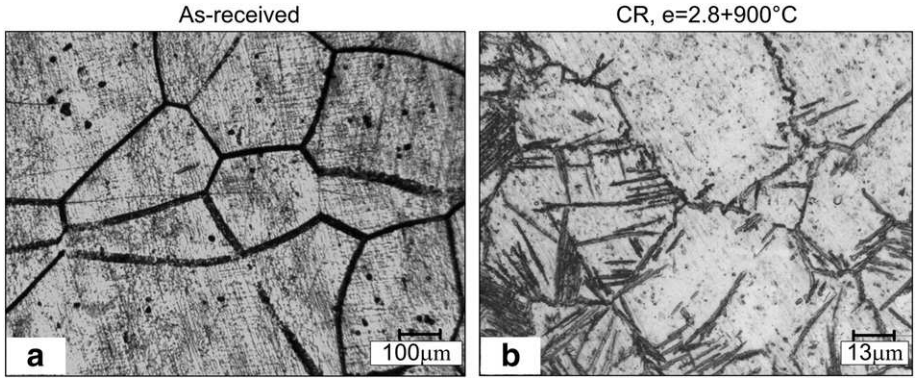

Fig. 13. Ti–18.1Nb–5Zr alloy microstructure before (a) and after (b) e = 2.75 cold rolling and 900 °C (1 h) annealing (optical microscopy).

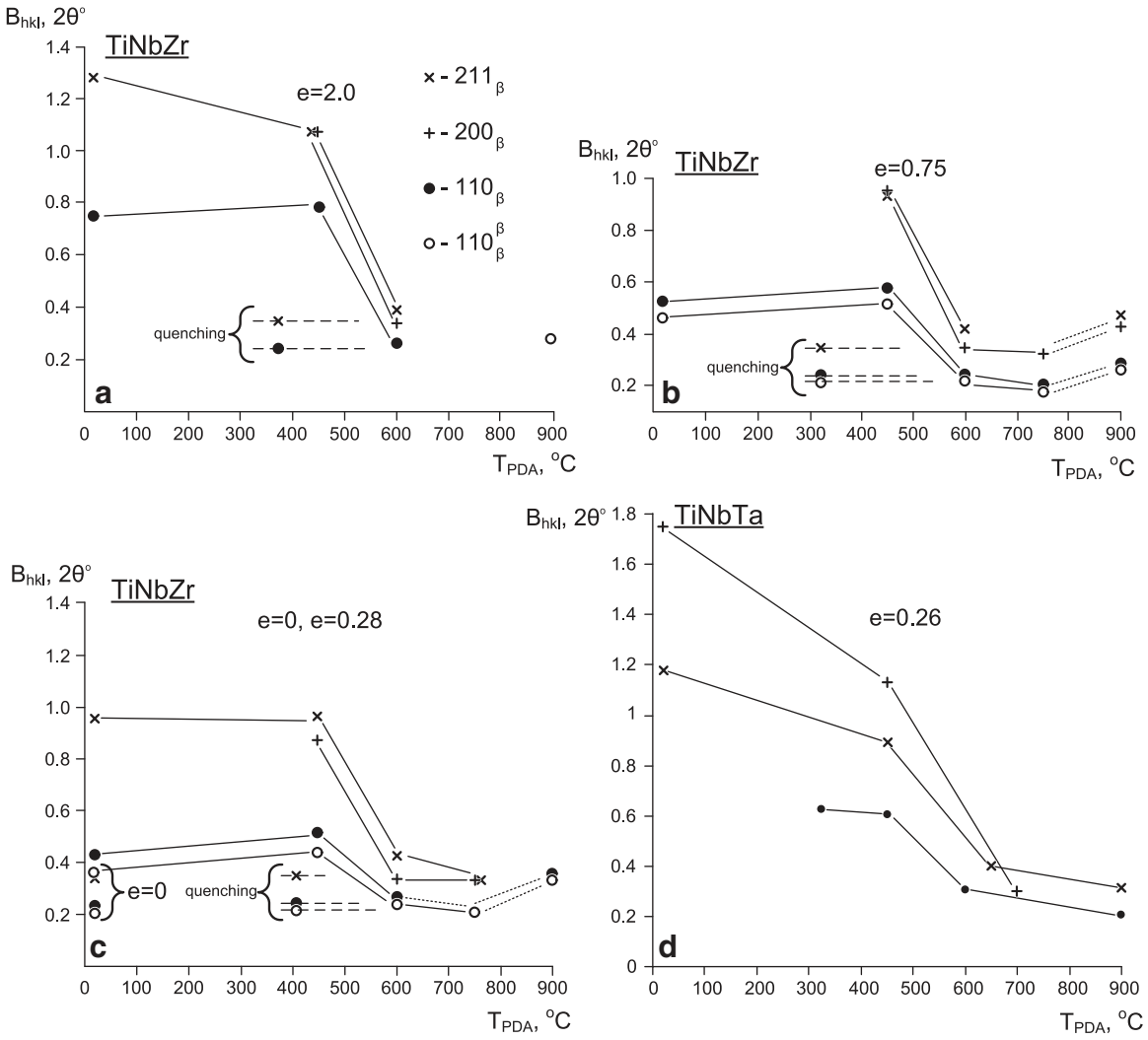

Fig. 14. Integral width of the β-austenite X-ray lines: (a, b, c) Ti–20.8Nb–5.5Zr and (d) Ti–19.5Nb–6.5Ta alloys as a function of annealing temperature after CR (110^{β}_{β} — in K_{β}-radiation).

annealing temperature, the higher the alloying element's solubility. An increase in the alloying element content will decrease the β→α transformation temperature till YS finally reaches its minimum when there is 100% of β-phase [36]. Further increase in the alloying elements' content will increase the strength of the β-material. In the vicinity of 600 °C, concurrence of the above-mentioned phenomena is superimposed on the low stability of the β-phase and therefore results in accentuated material softening.

It can be concluded that the selected composition and annealing (600 °C, 1 h) enable the β↔α″ transformation, leading to a superelastic behavior of the material with low Young modulus. Cold work results in an effective grain refinement, but does not significantly affect the alloy's stress-strain superelastic behavior.

4.2. Ti–Nb–Zr foams

4.2.1. Ti–Nb–Zr foams versus bones

Fig. 17 compares the mechanical behavior of the bovine trabecular bone [26–28,37] with that of Ti–Nb–Zr foam: the apparent Young's modulus matches perfectly that of the bone, but the CS^* is always higher, being about 70 MPa for the high-porosity samples of our study. One of the important characteristics of materials for orthopedic applications is the maximum elastic strain: for bone it is about 1.1%, for the high-porosity Ti–Nb–Zr specimens it is around 3%, which guarantees that the implant will not be damaged before the bone [26–28,37].

4.2.2. Mechanical behavior

Three main regions can generally be distinguished on the compression stress–strain diagram of metallic foams: (1) linear elasticity, which is generally attributed to walls bending, (2) elasto-plastic yielding attributed to cell walls' collapse (σ^*, see Fig. 17), and (3) progressive collapse and densification (see Figs. 10 and 17).

Generally speaking, the mechanical properties of porous metals satisfactorily agree with Gibson and Ashby's analytical models [38] when the metal porosity varies between 30 and 70% [39]. According to these models, the most important structural characteristic influencing the mechanical behavior of foams (apparent plateau stress and Young's modulus) is relative density, which is the absolute foam density (ρ^*) divided by the theoretical density, or the density of the solid (bulk) material (ρ_s).

Two different foam morphologies are generally distinguished: open-cell and closed-cell foams. These structures are characterized by different mechanical behaviors: (1) in open-cell foams, cell walls bend under load; and (2) in closed-cell foams, porous membranes stretch and bend and, in addition, compression of the cell fluid (air, liquid) trapped inside of cells contributes to the mechanical behavior of the material. Given that the metallic foams produced in this work are

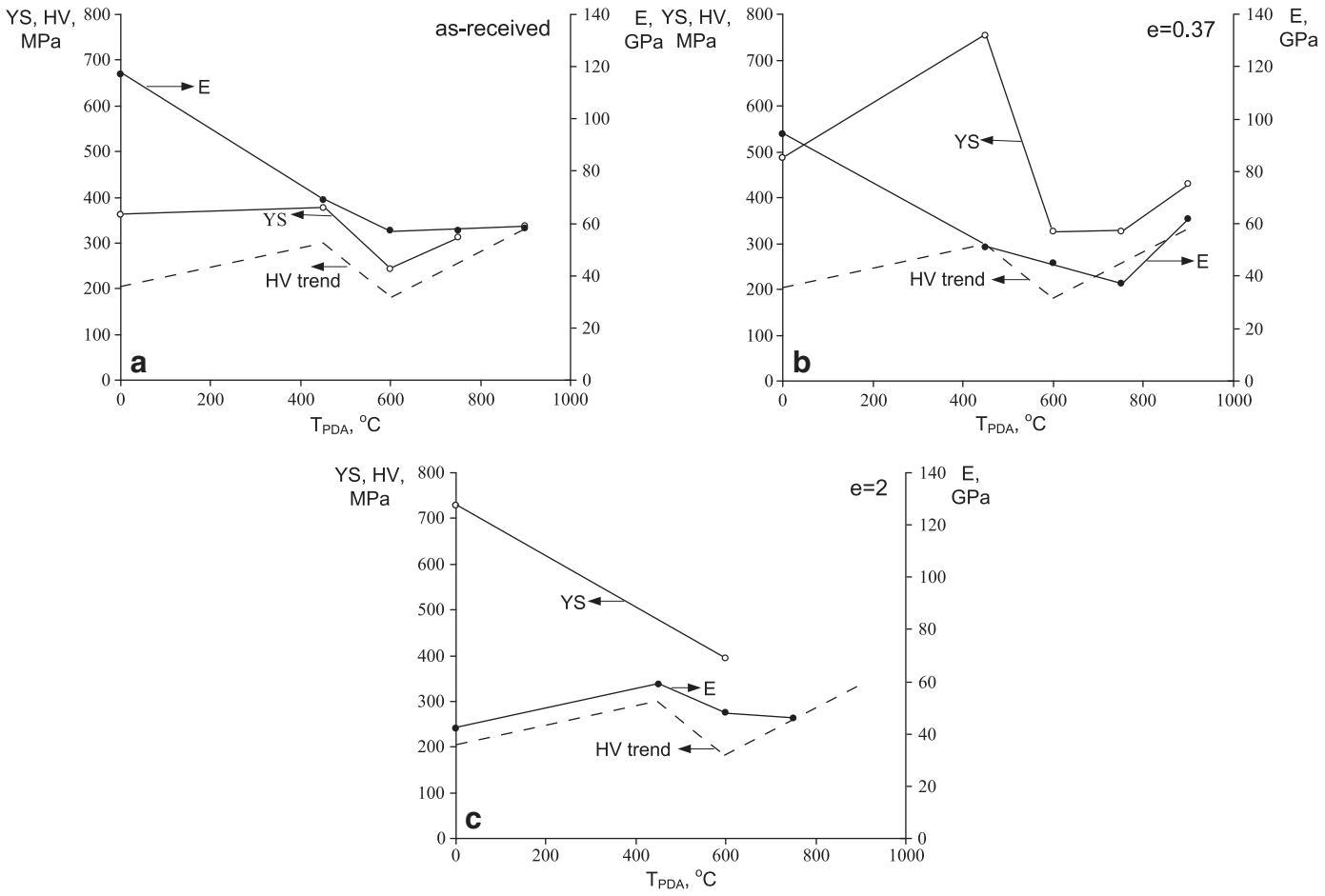

Fig. 15. Ti–20.5Nb–5.6Zr alloy: HV, YS and E trends in respect to annealing temperature: a) as-received; b) CR (e = 0.37); and c) CR (e = 2). HV trend is taken from Fig. 5b.

open-cell foams, the Gibson–Ashby analytical model of open-cell foams with regularly distributed cells will be used.

4.2.2.1. Plateau stress. The beginning of the plastic collapse in cellular materials is determined as follows [38]:

$$\frac{\sigma^*_{pl}}{\sigma_{ys}} = C_1\left(\frac{\rho^*}{\rho_s}\right)^{3/2}, \quad (1)$$

where σ^*_{pl} is the plastic collapse stress of the cellular foam, σ_{ys} is the yield stress of the cell edge material (solid material), and $C_1 \approx 0.3$ for cellular metals.

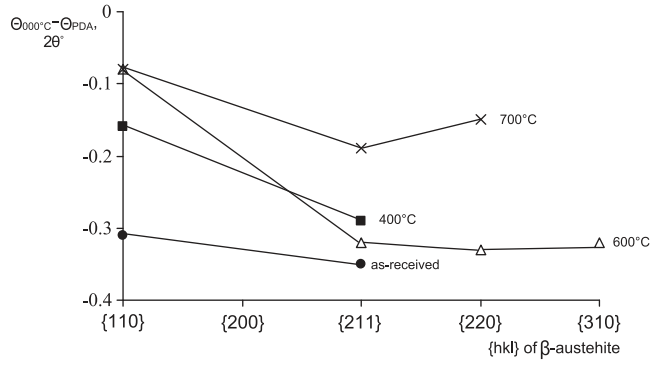

Fig. 16. Peak position shift of β-austenite lines in as-received samples as compared to annealing at 900 °C.

The elastic collapse stress can be expressed as follows [38]:

$$\frac{\sigma^*_{el}}{E_s} = C_2\left(\frac{\rho^*}{\rho_s}\right)^2, \text{so}\,\sigma^*_{el} = E_s C_2\left(\frac{\rho^*}{\rho_s}\right)^2, \quad (2)$$

where $C_2 \approx 0.05$ for cellular metals.

Note that in the case of extremely porous materials: $\frac{\rho^*}{\rho_s} < 36\left(\frac{\sigma_{ys}}{E_s}\right)^2$ elastic collapse could precede plastic collapse. For metals $\frac{\sigma_{ys}}{E_s} < \frac{1}{300}$, so the relative density should be less than 0.0004 to respect this condition, which is improbable. Thus, plastic collapse seems to be a dominant deformation mechanism in cellular metallic foams. Given the irregular structure of the foams used in this study however, two collapse mechanisms, plastic and elastic, could be activated simultaneously but to a different extent.

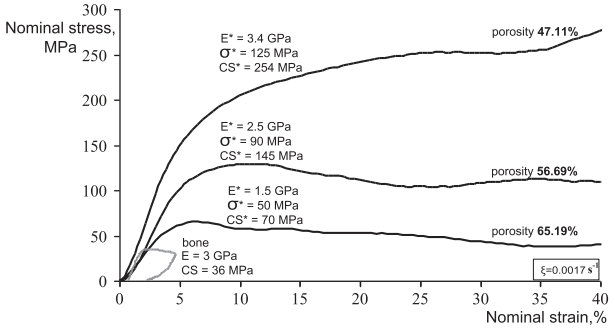

Fig. 17. Compression behavior of Ti–Nb–Zr foams and bovine trabecular bone [37].

The plastic and elastic collapse models for compressive stresses of foams can be combined using the rule of mixture to calculate the plateau stress of the foam [40]:

$$\sigma^* = f\sigma^*_{pl} + (1-f)\sigma^*_{el} = fC_1\sigma_{ys}\left(\frac{\rho^*}{\rho_s}\right)^{3/2} + (1-f)C_2E_s\left(\frac{\rho^*}{\rho_s}\right)^2, \quad (3)$$

where f represents the contribution (weight) of the plastic deformation mechanism to the compression plateau stress.

4.2.2.2. Young's modulus. For open-cell foams [38]:

$$\frac{E^*}{E_s} = A\left(\frac{\rho^*}{\rho_s}\right)^2, \quad (4)$$

where E^* and E_s are the apparent and true Young's moduli of foam and dense (bulk) material, respectively; ρ^*, ρ_s are the densities of foam and bulk material. $A \approx 1$ for cellular metals.

Considering the possibility of the elastic and plastic deformation occurring simultaneously from the very beginning of the foam deformation, we suppose that the apparent Young's modulus can also be represented as a weighted combination of two moduli: the elastic deformation slope and the plastic deformation plateau slope (hardening coefficient) of the bulk material. Using the rule of mixture, the apparent Young's modulus of the foams can therefore be expressed by the following equation:

$$E^* = fK\left(\frac{\rho^*}{\rho_s}\right)^2 + (1-f)AE_s\left(\frac{\rho^*}{\rho_s}\right)^2, \quad (5)$$

where f represents the contribution (weight) of plastic deformation mechanism to the apparent Young's modulus, and K is a hardening coefficient of the plastic plateau of the bulk materials. As can be observed on the stress–strain diagrams of Fig. 6a, K varies from 4 to 12 GPa for the as-received and annealed bulk samples of Ti–20.5Nb–5.6Zr alloy.

This hypothesis is indirectly confirmed by the metallographic analysis of compressed Cu-porous samples, which demonstrates that the apparently elastic zone on the diagram indeed reflects the mixed elasto-plastic behavior of the foam: during testing, spherical pores take partially irreversible ellipsoidal shape [41].

Application of both rule-of-mixture models (3, 5) to the results of the present study gives a good correlation between experimental and calculated data (Fig. 18).

It is clear that relative density is not the only parameter that influences the mechanical behavior of metallic foams. It also depends on the pores' size, shape and distribution, including detailed pore morphology, such as micro-pores forming at the edges [42]. As underlined in Ref. [40], pore shapes and sizes play a critical role in determining the compression behaviors of foams. In Ref. [41], for example, the yield stress dependence on the powder size was similar

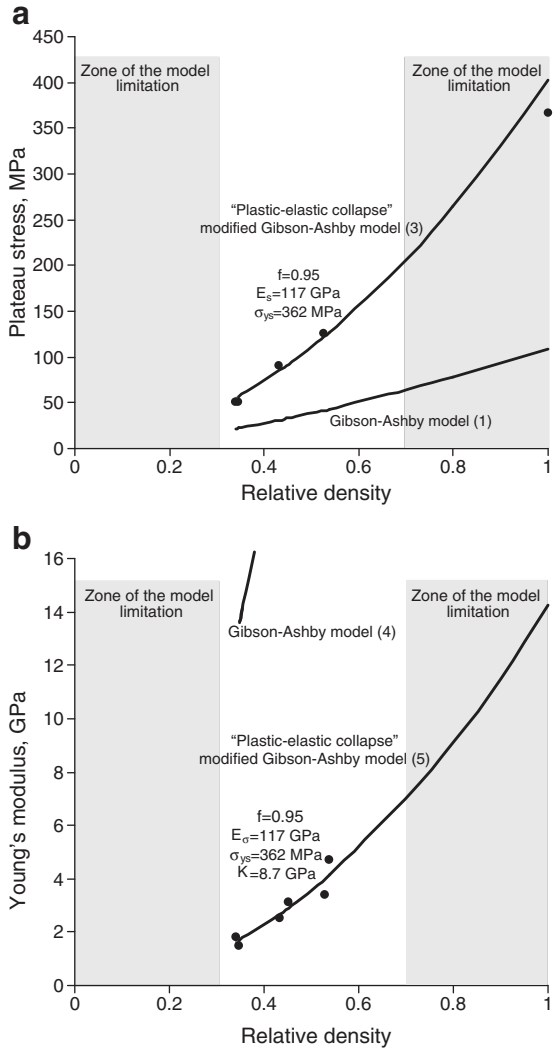

Fig. 18. Application of the modified Gibson–Ashby models to the analysis of Ti–Nb–Zr foams compression behavior: a) yield stress, and b) Young's modulus; shaded zones correspond to the zones of Gibson–Ashby models' limitations; hardening coefficient K and weight coefficient f are calculated by the least square method.

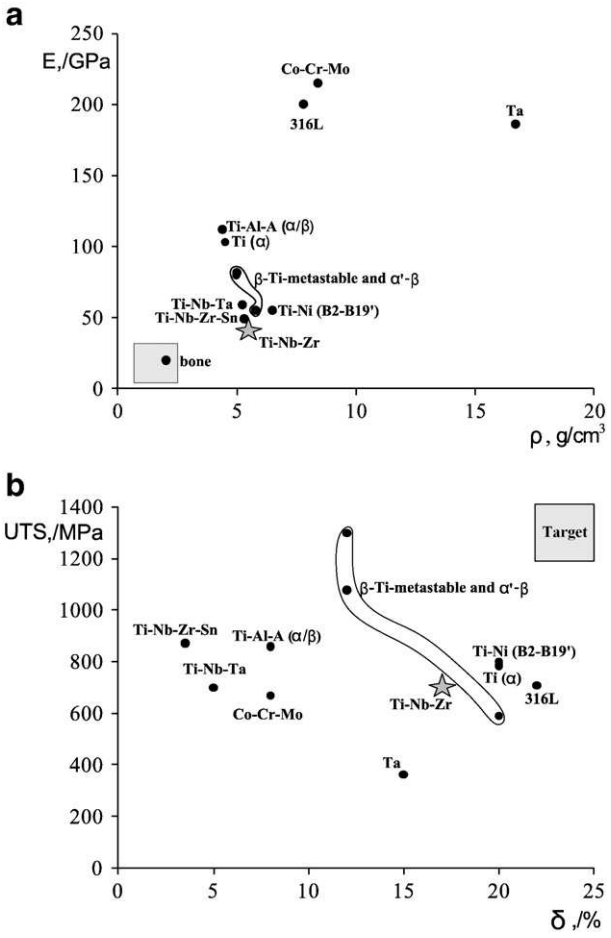

Fig. 19. a) Young's modulus versus density and b) UTS versus elongation; data obtained from Refs. [7,43–49]; "star" signs indicate the results of this study.

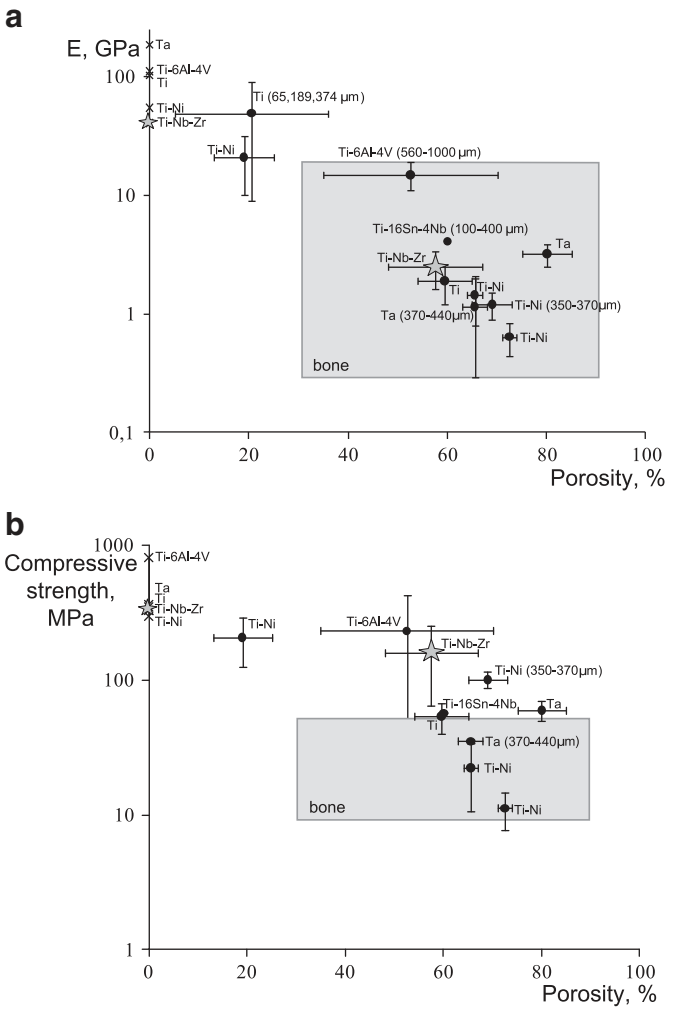

Fig. 20. a) Young's modulus and b) compressive strength versus porosity (in the parenthesis — pore size where known); data obtained from Refs. [47,48,50–53]; "star" signs indicate the results of this study.

to the Hall–Petch relationship, but that of the Young's modulus was found to be independent. That said, additional experimental validation is needed before we can conclude on the overall validity of this approach.

5. Conclusions

The characteristics of the bulk metallic materials for orthopedic applications are collected in Fig. 19. It can be seen that the Ti–Nb–Zr alloy developed in this study represents one of the closest to human bone combinations of the "Young's modulus-density" properties (Fig. 19a), compared to the metallic materials already used in orthopedics, such as Ta, Co–Cr–Mo, 316L, etc. From the combined "UTS-elongation" point of view, Ti–Nb–Zr alloys are situated in the zone of average UTS, with better ductility than Co–Cr–Mo and Ta (Fig. 19b) [43–49].

Some of the mechanical characteristics of porous metallic materials for orthopedics are presented in Fig. 20. It is clear that Ti–Nb–Zr porous alloy demonstrates a competitive combination of "Young's modulus–Porosity" properties relative to human bones as compared to the known metallic foams, such as Ta, Ti–Ni, etc. From the "Compressive strength–Porosity" point of view, Ti–Nb–Zr foams are situated higher than the "Strength–Porosity" region for human bone, thus ensuring safe utilization of these foams as bone replacement materials [47,48,50–53].

The following points summarize the main results of this study:

1. The Young's modulus of bulk ternary near-beta Ti–Nb–Zr(Ta) alloys (E = 45–55 GPa) comes close to that of cortical human bones. This quality makes them a prospective candidate for orthopedic implants, such as hip prosthesis stems.
2. Annealing at 600 °C (1 h) after all cold work intensities corresponds to the minima in strength and Young's modulus of bulk TiNbZr(Ta) alloys. This softening phenomenon can be explained by the stress-induced martensitic transformation. Cold work results in an effective grain refinement, but does not significantly affect the alloy's stress–strain superelastic behavior.
3. The Young's modulus of the porous Ti–Nb–Zr alloy samples varies from 1.5 to 5 GPa depending on the porosity, which is close to this parameter in trabecular human bones. Compressive stress before failure is at least two times higher than the same bone parameter, thus ensuring safe utilization of the foams as implant materials from a mechanical point of view.
4. A modified Gibson–Ashby model for the cellular solids allows good prediction of the mechanical properties of the Ti–Nb–Zr foams studied in this work.
5. Generally speaking, the stress–strain relationship of bulk metastable beta Ti–Nb–Zr alloys is comparable with the best concurrent low-modulus Ti-based alloys, whereas the pore size and mechanical properties of foams produced from these alloys are comparable to concurrent metallic foams for medical applications.

Acknowledgments

The authors would like to express their gratitude to Dr S. Miyazaki and Dr K. Kim from Tsukuba University (Japan) and to Dr L.-P. Lefebvre and Dr E. Baril from the NRC Industrial Materials Institute (Canada) for useful discussions. This work was supported by the Ministry of Economic Development of Quebec, the National Science and Engineering Research Council of Canada and the Ministry of Education and Science of the Russian Federation.

References

[1] O. Prymak, D. Bogdanski, M. Koller, S. Esenwein, G. Muhr, F. Beckmann, T. Donath, M. Assad, M. Epple, Biomater 26 (29) (2005) 5801.
[2] Ryhänen, Biocompatibility evaluation of nickel–titanium shape memory alloy, Academic Dissertation, University of Oulu, 1999.
[3] K. Takamura, K. Hayashi, N. Ishinishi, T. Yamasda, Y. Sugioka, J. Biomed. Mater. Res. 28 (5) (1980) 583.
[4] H.Y. Kim, Y. Ikehara, J.I. Kim, H. Hosoda, S. Miyazaki, Acta Mater. 54 (9) (2006) 2419.
[5] S. Miyazaki, H.Y. Kim, H. Hosoda, Mater. Sci. Eng., A 438–440 (2006) 18.
[6] Y.L. Hao, S.J. Li, S.Y. Sun, C.Y. Zheng, Q.M. Hu, R. Yang, Appl. Phys. Lett. 87 (9) (2005), 91906-1-3.
[7] S.J. Li, T.C. Cui, Y.L. Hao, R. Yang, Acta Biomater. 4 (2008) 305.
[8] E. Takahashi, T. Sakurai, S. Watanabe, N. Masahashi, S. Hanada, Mater. Trans. 43 (2002) 2978.
[9] L.C. Zhang, T. Zhou, S.P. Alpay, M. Aindow, M.H. Wu, Appl. Phys. Lett. 87 (2005), 241909-1-3.
[10] M.I. Petrzhik, S.G. Fedotov, Proc. XVI Conf. on Applied Crystallography, World Sci. Pbl., , 1995, p. 273.
[11] A.K. Mishra, J.A. Davidson, P. Kovacs, R.A. Poggie, in: D. Eylon, R.R. Boyer, D.A. Koss (Eds.), Beta Titanium in the 1990's, TMS, Warrendale, PA, 1993, p. 61.
[12] M. Niinomi, Biomater 24 (2003) 2673.
[13] R. Brånemark, B. Rydevik, R. Myers, P.-I. Brånemark, J. Rehabil. Res. Dev. 38 (2) (2001) 175.
[14] J.T. Clemow, A.M. Weinstein, J.J. Klawitter, J. Biomed. Mater. Res. 15 (1) (1981) 73.
[15] W. Pompe, H. Worch, M. Epple, W. Friess, M. Gelinsky, P. Greil, U. Hempel, D. Scharnweber, K. Schulte, Mater. Sci. Eng., A 362 (1–2) (Dec. 5 2003) 40.
[16] R. Menini, M.-J. Dion, Siu Kee Vicky So, M. Gauthier, L.-Ph. Lefebvre, J. Electrochem. Soc. 153 (1) (2006) B13.
[17] X. Wang, Y. Li, et al., Acta Biomater. 5 (9) (2009) 3616.
[18] M. Morinaga, Y. Murata, H. Yukawa, in: G. Bozzolo, R.D. Noebe, P.B. Abel (Eds.), Applied Computational Materials Modeling: Theory, Simulation and Experiment, Springer, 2007, p. 255.
[19] M. Abdel-Hady, K. Hinoshita, M. Morinaga, Scr. Mater. 55 (2006) 477.
[20] M. Abdel-Hady, H. Fuwa, K. Hinoshita, H. Kimura, Y. Shinzato, M. Morinaga, Scr. Mater. 57 (2007) 1000.

[21] United States Patent Number 6, 660, 224 (US Patent Application Serial Number 09/938, 638) filed August 27, 2001, titled "Method of Making Open Cell Material" by inventors Louis-Philippe Lefebvre and Yannig Thomas.
[22] I.I. Kornilov, N.F. Zhebyneva, S.V. Oleynikova, L.P. Fatkullina, I.I. Kornilov, N.F. Zhebyneva, S.V. Oleynikova, L.P. Fatkullina, Proc. Int. Conf. ICOMAT-77, 1978,, Kiev.
[23] H.C. Lin, S.K. Wu, Metall. Trans. 24A (2) (1993) 293.
[24] V. Brailovski, S.D. Prokoshkin, I.Yu. Khmelevskaya, K.E. Inaekyan, V. Demers, S.V. Dobatkin, E.V. Tatyanin, Mater. Trans. 47 (3) (2006) 795.
[25] S.D. Prokoshkin, V. Brailovski, K.E. Inaekyan, V. Demers, I.Yu. Khmelevskaya, S.V. Dobatkin, E.V. Tatyanin, Mater. Sci. Eng., A 481–482 (2008) 114.
[26] J.E. Lemons, Quantitative Characterization and Performance of Porous Implants for Hard Tissue Applications, ed. ASTM, STP953, 1987.
[27] J.D. Bobyn, M. Tanzer, J.E. Miller, in: B.F. Morrey (Ed.), Reconstructive Surgery of the Joints, Churchill Livingstone, New York, 1995, p. 75.
[28] K.H. Frosh, F. Barvencik, V. Viereck, C.H. Lohmann, K. Dresing, J. Breme, E. Brunner, K.M. Strumen, J. Biomed. Mater. Res. 68 A (2) (2004) 325.
[29] H.Y. Kim, S. Hashimoto, J.I. Kim, T. Inamura, H. Hosoda, S. Miyazaki, Mater. Sci. Eng., A 417 (2006) 120.
[30] E.W. Collings, Titanium alloys, ed. A.S.f. Metals. 1984.
[31] K.C. Hari Kumar, P. Wollants, L. Delaey, J. Alloys Compd. 206 (1994) 121.
[32] A. Inoue, T. Wada, X.M. Wang, A.L. Greer, Mater. Sci. Eng., A 442 (2006) 233.
[33] Y. Ohmori, T. Ogo, K. Nakai, S. Kobayashi, Mater. Sci. Eng., A 312 (2001) 182.
[34] T. Ahmed, H.J. Rack, J. Mater. Sci. 31 (1996) 4267.
[35] Y.-L. Zhou, M. Niinomi, J. Alloys Compd. 466 (2008) 535.
[36] C.R. Brooks, American society for metals, USA, 1982.
[37] T.L.A. Moore, L.J. Gibson, J. Biomech. Eng. 124 (2002) 63.
[38] L.J. Gibson, M.F. Ashby, L.J. Gibson, M.F. Ashby, Cellular Solids: Structure and Properties, 2nd edition ed., Cambridge University Press, 1999.
[39] C.E. Wen, M. Mabuchi, Y. Yamada, K. Shimojima, Y. Chino, T. Asahina, Scr. Mater. 45 (2001) 1147.
[40] C. Zou, E. Zhang, M. Li, S. Zeng, J. Mater. Sci. - Mater. Med. 19 (2008) 401.
[41] E. Zhang, B. Wang, Int. J. Mech. Sci. 47 (2005) 744.
[42] L.J. Gibson, J. Biomech. 18 (5) (1985) 317.
[43] M. Niinomi, Mater. Sci. Eng., A 243 (1998) 231.
[44] M. Long, H.J. Rack, Biomater 19 (1998) 1621.
[45] E.B. Taddei, V.A.R. Henriques, C.R.M. Silva, C.A.A. Cairo, Mater. Sci. Eng., C 24 (2004) 683.
[46] A. Schuh, J. Bigoney, W. Honle, G. Zeiler, U. Holzwartg, R. Forst, Materialwiss. Werkstofftech. 38 (12) (2007) 1003.
[47] B.R. Levine, S. Sporer, R.A. Poggie, C.J. Della Valle, J.J. Jacobs, Biomater 27 (2006) 4671.
[48] L.D. Zardiackas, D.E. Parsell, L.D. Dillon, D.W. Mitchell, L.A. Nunnery, R. Poggie, J. Biomed. Mater. Res. 58 (2) (2001) 180.
[49] V. Brailovski, S. Prokoshkin, P. Terriault, F. Trochu (Eds.), Shape Memory Alloys: Fundamentals, Modeling and Application, 1ère ed., École de Technologie Supérieure, Montréal, 2003.
[50] A. Nouri, X.B. Chen, P.D. Hodgson, C.E. Wen, Adv. Mater. Res. 15–17 (2007) 71.
[51] I.-H. Oh, N. Nomura, N. Masahashi, S. Hanada, Scr. Mater. 49 (2003) 1197.
[52] O. Scalzo, S. Turenne, M. Gauthier, V. Brailovski, Metall. Mater. Trans. A 40 (2009) 2061.
[53] A. Chernyshov, M. Leroux, M. Assad, A. Dujovne, E. Garcia-Belenguer, Adv. Mater. Biomed. Appl. Montreal: Met. Soc. (2002) 109.